

# Supporting Information

## Quantum Theory of Electronic Excitation and Sputtering by Transmission Electron Microscopy

Anthony Yoshimura<sup>1,2\*</sup>, Michael Lamparski<sup>2</sup>, Joel Giedt<sup>2</sup>,  
David Lingerfelt<sup>3</sup>, Jacek Jakowski<sup>3</sup>, Panchapakesan Ganesh<sup>3</sup>, Tao Yu<sup>4</sup>,  
Bobby Sumpter<sup>3</sup>, and Vincent Meunier<sup>2,5</sup>

<sup>1</sup>*Lawrence Livermore National Laboratory, Livermore, CA 94550, USA*

<sup>2</sup>*Department of Physics, Applied Physics, and Astronomy, Rensselaer Polytechnic Institute,  
Troy, New York 12180, USA*

<sup>3</sup>*Center for Nanophase Material Sciences, Oak Ridge National Laboratory, Oak Ridge, TN  
37831, USA*

<sup>4</sup>*Department of Chemistry, University of North Dakota, Grand Forks, ND 58202, USA*

<sup>5</sup>*Department of Materials Science and Engineering, Rensselaer Polytechnic Institute, Troy,  
NY 12180, USA*

<sup>\*</sup>*Correspondence to be addressed to yoshimura4@llnl.gov*

### S1 Invariant matrix element $\mathcal{M}$

As the excitation amplitude in equation (16) contains the invariant matrix element  $\mathcal{M}$  and not  $|\mathcal{M}|^2$ , we are unable to use the spin sum identities typically used to derive cross sections in quantum electrodynamics.<sup>1,2</sup> Nonetheless, the evaluation of  $\mathcal{M}$  in equation (4) is straightforward, though a bit cumbersome. In the Dirac basis,<sup>3</sup>

$$\gamma^0 = \begin{pmatrix} I & 0 \\ 0 & -I \end{pmatrix} \quad \text{and} \quad \gamma^i = \begin{pmatrix} 0 & \sigma^i \\ -\sigma^i & 0 \end{pmatrix}, \quad (\text{S1})$$

where

$$I = \begin{pmatrix} 1 & 0 \\ 0 & 1 \end{pmatrix} \quad \text{and} \quad \vec{\sigma} = \left\{ \begin{pmatrix} 0 & 1 \\ 1 & 0 \end{pmatrix}, \begin{pmatrix} 0 & -i \\ i & 0 \end{pmatrix}, \begin{pmatrix} 1 & 0 \\ 0 & -1 \end{pmatrix} \right\}. \quad (\text{S2})$$

The electron spinors in equation (4) can be written as

$$u^1(p) = \sqrt{\epsilon + m} \begin{pmatrix} 1 \\ 0 \\ \frac{p^z}{\epsilon + m} \\ \frac{p^x + ip^y}{\epsilon + m} \end{pmatrix} \quad \text{and} \quad u^2(p) = \sqrt{\epsilon + m} \begin{pmatrix} 0 \\ 1 \\ \frac{p^x - ip^y}{\epsilon + m} \\ \frac{-p^z}{\epsilon + m} \end{pmatrix}, \quad (\text{S3})$$

while

$$\bar{u}^s(p) = u^{s\dagger}(p)\gamma^0. \quad (\text{S4})$$

As justified in section 2.1.1, we need only evaluate the t-channel contribution to  $\mathcal{M}$  and multiply the result by 2. That is,

$$\mathcal{M}(p_4 p_3 \leftarrow p_2 p_1) \sim e^2 \sum_{s_1, s_2, s_3, s_4} \bar{u}^{s_4}(p_4) \gamma^\mu u^{s_1}(p_1) \left( \frac{1}{p_3 - p_2} \right)^2 \bar{u}^{s_3}(p_3) \gamma_\mu u^{s_2}(p_2). \quad (\text{S5})$$

Substituting equations (S1) through (S4) into (S5) yields  $\mathcal{M}$  in terms of the components of the electrons' 4-momenta. That is,

$$\begin{aligned} \mathcal{M}(p_4 p_3 \leftarrow p_2 p_1) \sim & -\frac{2e^2}{(p_3 - p_2)^2} [(\epsilon_1 + m)(\epsilon_2 + m)(\epsilon_3 + m)(\epsilon_4 + m)]^{-1/2} \\ & \times \left\{ (\epsilon_1 + m)p_4^x [(\epsilon_2 + m)p_3^x + (\epsilon_3 + m)p_2^x] \right. \\ & + 2(\epsilon_1 + m)(\epsilon_3 + m)(p_2^y + ip_2^z)(p_4^y - ip_4^z) \\ & + 2(\epsilon_2 + m)(\epsilon_4 + m)ip_1^z(p_3^y - ip_3^z) \\ & - [(\epsilon_2 + m)(\epsilon_3 + m) + p_2^x p_3^x + (p_2^y + ip_2^z)(p_3^y - ip_3^z)] \\ & \left. \times [(\epsilon_1 + m)(\epsilon_4 + m) + ip_1^z(p_4^y - ip_4^z)] \right\}, \quad (\text{S6}) \end{aligned}$$

where we let  $p_1$  denote the momentum of the beam electron so that  $p_1^x = p_1^y = 0$ . See the Mathematica<sup>4</sup> notebook in the Supporting Information for more details.

## S2 Normalization

When integrating over 4-momentum space as is done in section 2.1.2, Lorentz invariance constrains a particle's 4-momentum to obey  $p^2 = m^2$ . It follows that the 4-momentum integration measure  $d^4p$  is always multiplied by a delta function  $\delta(p^2 - m^2)$ , *i.e.*,

$$d^4p \delta(p^2 - m^2) \theta(p^0) = \frac{d^4p}{2p^0} \delta(p_0 - \epsilon_{\mathbf{p}}), \quad (\text{S7})$$

where the Heaviside step function restricts our consideration to particles of positive mass (we note that antiparticles are interpreted as positive mass particles that propagate backwards in time). With this integration measure, the identity operator can be written as

$$\begin{aligned} \hat{I} &= \int \frac{d^4p}{(2\pi)^4} (2\pi) \delta(p^2 - m^2) \theta(p^0) |p\rangle \langle p| \\ &= \int \frac{d^3p}{(2\pi)^3 2\epsilon_{\mathbf{p}}} |p\rangle \langle p| \\ &= \int \frac{d^3p}{(2\pi)^3} |\mathbf{p}\rangle \langle \mathbf{p}|. \end{aligned} \quad (\text{S8})$$

The last equality implies that

$$|p\rangle = (2\epsilon_{\mathbf{p}})^{1/2} |\mathbf{p}\rangle. \quad (\text{S9})$$

### S3 Lab frame $p_3^z$

For the scattering of two free electrons, conservation of 4-momentum allows us to write

$$p_1 + p_2 = p_3 + p_4. \quad (\text{S10})$$

This constrains four of the six components needed to specify the 3-momenta of the two outgoing particles, so that only two components are independent. We choose the independent components to be  $p_3^x$  and  $p_3^y$ . Thus, we wish to find  $p_3^z$  as a function of  $p_1$ ,  $p_2$ ,  $p_3^x$ , and  $p_3^y$ . From this,  $p_4 = p_1 + p_2 - p_3$  is easily obtained, and we have all six components of outgoing 3-momenta needed to calculate the scattering amplitude from equation (16). We start by setting the  $z$ -direction parallel to  $\mathbf{p}_1$ . This means that

$$\begin{aligned} p_4^x &= p_2^x - p_3^x \\ p_4^y &= p_2^y - p_3^y \\ p_4^z &= p_1^z + p_2^z - p_3^z \\ \epsilon_4 &= \epsilon_1 + \Delta\epsilon \end{aligned} \quad (\text{S11})$$

where

$$\epsilon_i = \epsilon_{\mathbf{p}_i} = \sqrt{\mathbf{p}_i^2 + m^2}, \quad \Delta\epsilon = \epsilon_{n\mathbf{k}} - \epsilon_{n'\mathbf{k}'}, \quad (\text{S12})$$

and  $\epsilon_{n\mathbf{k}}$  and  $\epsilon_{n'\mathbf{k}'}$  are the eigenvalues of the excited hole and electron states, respectively. We can also write  $\epsilon_1 = \gamma m$  where  $\gamma = 1/\sqrt{1 - \beta^2}$  is the Lorentz factor corresponding to the beam electron's velocity  $\beta$ . Squaring the last line in (S11) and subtracting  $m^2$  then gives

$$\mathbf{p}_4^2 = \mathbf{p}_1^2 + 2\gamma m \Delta\epsilon + \mathcal{O}(\Delta\epsilon^2). \quad (\text{S13})$$

We can ignore terms of order  $\mathcal{O}(\Delta\epsilon^2)$  since  $\Delta\epsilon \ll m$ . Meanwhile, squaring and summing the first three equations in (S11) tells us that

$$\mathbf{p}_4^2 = \mathbf{p}_1^2 + \mathbf{p}_2^2 + \mathbf{p}_3^2 + 2[p_1^z p_2^z - \mathbf{p}_2^\perp \cdot \mathbf{p}_3^\perp - (p_1^z + p_2^z)p_3^z], \quad (\text{S14})$$

where the  $\perp$  superscript denotes the projection perpendicular to  $\hat{z}$ . Subtracting equation (S14) from equation (S13) then yields

$$0 \sim \mathbf{p}_2^2 + \mathbf{p}_3^2 + 2[p_1^z p_2^z - \mathbf{p}_2^\perp \cdot \mathbf{p}_3^\perp - (p_1^z + p_2^z)p_3^z] - 2\gamma m \Delta\epsilon. \quad (\text{S15})$$

Asymptotic formula (S15) can then be solved for  $p_3^z$ , so that

$$p_3^z \sim p_1^z + p_2^z \pm \sqrt{(p_1^z)^2 - (\mathbf{p}_2^\perp - \mathbf{p}_3^\perp)^2 + 2\gamma m \Delta\epsilon}. \quad (\text{S16})$$

We choose the  $-$  from  $\pm$  as we impose that  $\mathbf{p}_3$  is a component of the outgoing crystal electron state, whose  $z$ -momentum is much smaller than that of the beam electron.

## S4 Converging $n_i^{\max}$

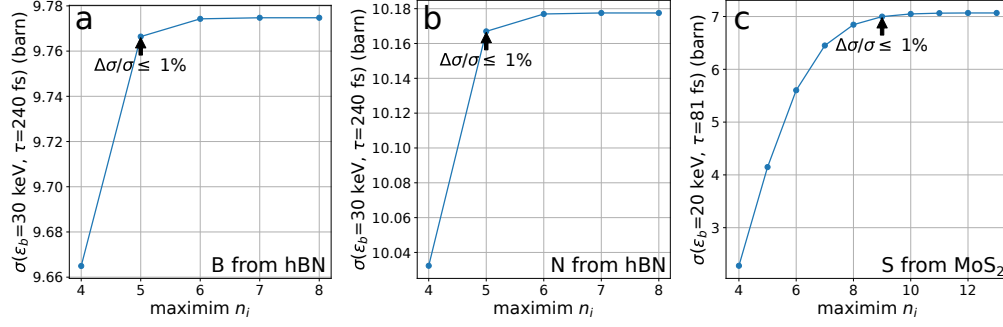


Figure S1: Convergence of the sputtering cross section with respect to the maximum number of beam-induced excitations  $n_i^{\max}$  considered. The simulated beam energies  $\epsilon_b$  are the lowest experimental beam energies used for each material. The excitation lifetimes  $\tau$  are those used to fit the experimental data in figures 5 and 6. Each cross section is deemed converged when any increase in  $n_i^{\max}$  increases the cross section by less than 1%.

## S5 Peaks in the sputtering cross section of hBN



Figure S2: The sputtering cross sections of boron and nitrogen from the hBN armchair edge peak at beam energies much lower than those typically used for microscopy and defect engineering. However, as mentioned in the main text, the validity of our perturbative approximation to the scattering operator breaks down at low beam energies (section 2.1.4). Thus, the values and positions of these peaks may change if higher order perturbation terms are considered.

## S6 Fitting and converging $S$

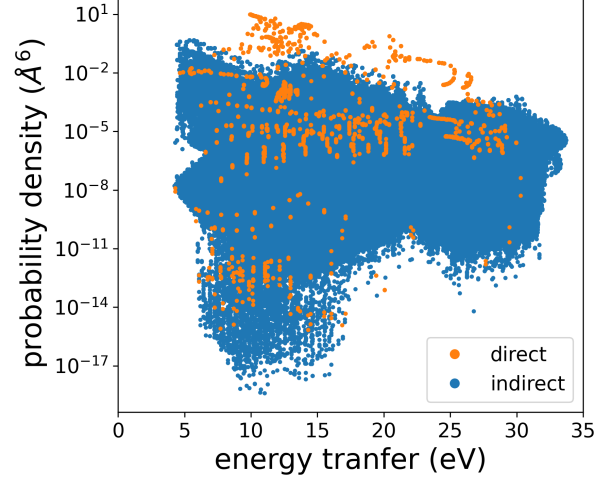


Figure S3: The most probable beam-induced electronic excitations are direct transitions. Each circle denotes the probability density centered on a particular excitation instigated by a 40 keV beam electron in hexagonal boron nitride, whose Brillouin zone was sampled by a  $18 \times 18 \times 1$  Monkhorst-Pack mesh.

Because the square of the momentum transfer appears in the denominator of the  $t$ -channel in equation (4), the probability density for electronic excitation peaks sharply when the momentum transfer is minimized. This minimization occurs when the beam electron induces a direct transition, in which the resulting electron and hole lie on the same k-point. Thus, direct excitations that conserve crystal momentum tend to be much more likely than indirect excitations (figure S3).

As a result, a sparse k-point mesh leads to an overestimation of  $S$ , the sum of all transition probabilities defined in equation (18). This is because a coarser k-point mesh yields a higher proportion of direct transitions, as there are fewer indirect transitions available for each k-point. For a given number of k-points  $N_k$ , the number indirect transitions is proportional to  $N_k$ , while the number of indirect transitions is proportional to  $N_k^2$ . Thus, increasing  $N_k$  increases the proportion of possible indirect transitions, lowering  $S$ . For a sufficiently dense mesh, the distinction between direct and nearly direct transitions is inconsequential, in which case,  $S$  is converged with respect to  $N_k$ .

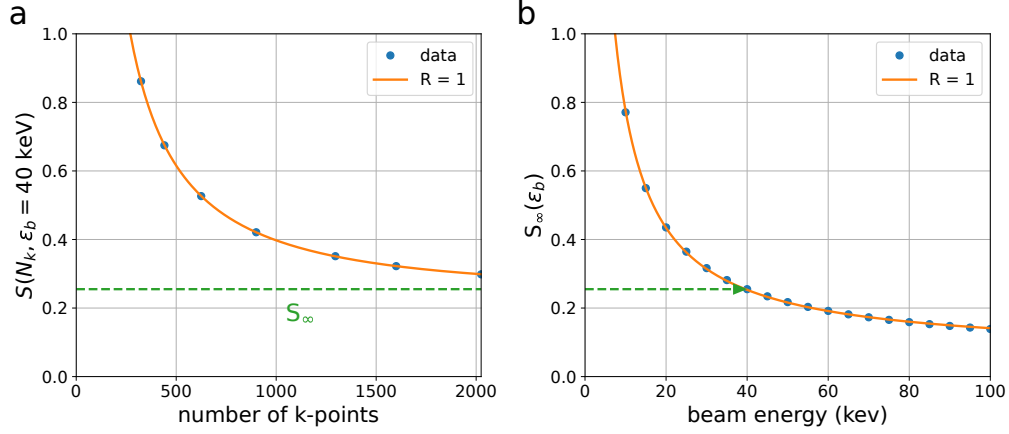


Figure S4: Finding the large crystal limit of  $S(\epsilon_b)$  requires extrapolation. Panel (a) shows the dependence of  $S$  on the number k-points  $N_k$  in the Brillouin zone of hBN under 40 keV irradiation. The simulated points are fitted well by equation (S17). The green dashed line denotes  $S_\infty$ , the asymptotic limit of  $S(N_k)$  for large  $N_k$ . Panel (b) then shows the dependence of  $S_\infty$  on the beam energy  $\epsilon_b$ , which is fitted well by equation (S18). The green arrow in panel (b) illustrates how  $S_\infty(\epsilon_b = 40 \text{ keV})$  is determined by the fit in panel (a).

Satisfactory convergence of  $S$  requires an extremely dense k-point mesh. We therefore use extrapolation to determine the converged value of  $S$ . For a given beam energy  $\epsilon_b$ , we calculate  $S$  for various  $N_k$ . We then fit the points to a curve of the form

$$S(N_k, \epsilon_b) = \frac{a}{N_k - b} e^{-cN_k} + S_\infty, \quad (\text{S17})$$

where  $a$ ,  $b$ ,  $c$ , and  $S_\infty$  are all fitting parameters that depend on  $\epsilon_b$  (figure S4a). The last parameter  $S_\infty$  is the limit of  $S$  for large  $N_k$ , and is taken as the converged value of  $S$  for that beam energy. We repeat this for multiple values of  $\epsilon_b$  ranging from 5 to 100 keV and record the best fit  $S_\infty$  for each  $\epsilon_b$ . Based on the work of Bethe,<sup>5-7</sup> we fit the resulting values of  $S_\infty(\epsilon_b)$  to an inverse function,

$$S_\infty(\epsilon_b) = \frac{A}{\epsilon_b - B} + C. \quad (\text{S18})$$

where  $A$ ,  $B$ , and  $C$  are fitting parameters. The parameters for hBN and MoS<sub>2</sub> are given in table S1. The fitted curve can then be substituted for  $S(\epsilon_b)$  in formula (23) to obtain  $P_i(\epsilon_b, n_i)$ , the probability of exciting  $n_i$  electrons in the large crystal limit.

Finally,  $S$  is also converged with respect to all other parameters. These include the maximum virtual photon momentum, DFT cutoff energy, and height of the pristine unit cell (figure S5).  $S$  is considered converged with respect to a parameter when any increase in the parameter's precision changes  $S$  by less than 5%.



material	A (eV)	B (eV)	C
hBN	7.655	-0.770	0.06526
MoS <sub>2</sub>	49.05	-3.867	0.3547

Table S1: Fitting parameters of equation (S18) for hBN and MoS<sub>2</sub>.

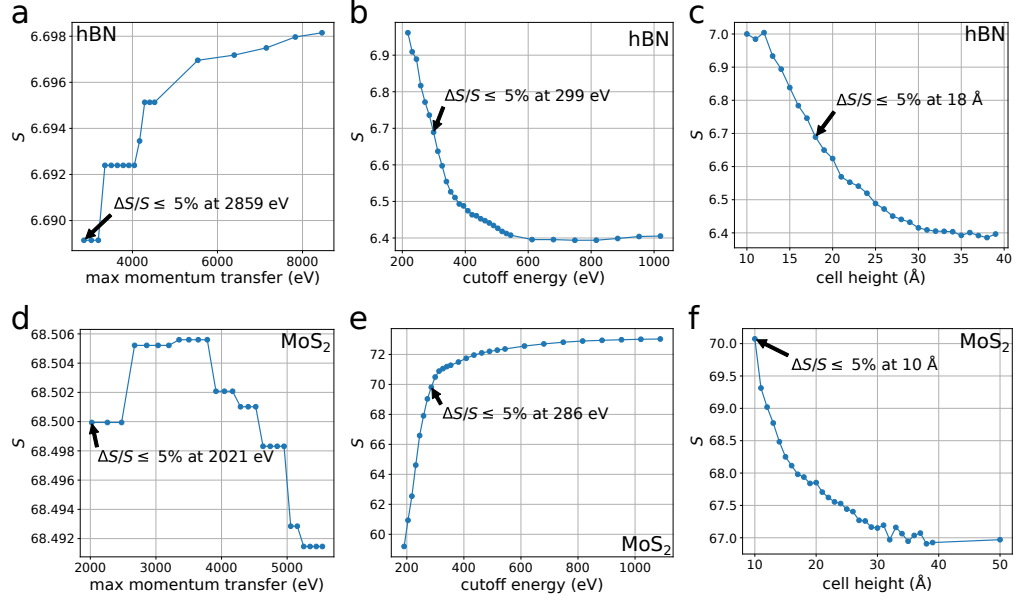


Figure S5: Convergence of  $S$  with respect to the (a and d) maximum magnitude of virtual photon momentum considered, (b and e) plane-wave DFT cutoff energy, and (c and f) height of the unit cell. A  $6 \times 6 \times 1$  k-point mesh and a beam energy of 60 keV is used to generate all six plots. The converged parameters were found to be insensitive to changes in k-point density and beam energy.  $S$  is deemed converged when any increase in precision changes  $S$  by less than 5%.

## S7 Validity of the three simplifying assumptions

While the three assumptions laid out in section 2.2.1 may seem drastic, their affect on the sputtering cross section is small due to a cancellation of errors. To see this, consider the connection between the potential energy surfaces (ESs) and the PKA velocity. By assumption 1, the ESs at the PKA's initial position are equally spaced, separated by the material's band gap. By assumption 2, the ESs converge to the same energy as the PKA approaches a distance  $d$ . We shall ignore assumption 3 for now. If we consider that the ESs are not constant as the PKA moves towards  $d$ , so that the PKA slows down in transit, then the energy required to get to  $d$  depends on when the system relaxes to a lower ES. This is because higher ESs have shallower slopes than do the lower ones, so the PKA's deceleration will be smaller while on a higher ES. Thus, as the PKA moves, the ESs converge by assumption 2, and the energy lost during relaxation tends to shrink.

By introducing assumption 3, the energy lost during relaxation does not shrink but remains constant while the PKA sputters, and is therefore generally greater than it would be with gradually changing ESs. Our method therefore overestimates the energy lost during relaxation. On the other hand, because the PKA does not slow down until it reaches  $d$ , assumption 3 also underestimates the sputtering time  $t_s$ , introduced in equation (25). A smaller  $t_s$  means that fewer excitations relax during sputtering, increasing the cross section. However, each relaxation comes at a higher energy cost, which makes the PKA less likely to overcome the displacement threshold, decreasing the cross section. Thus, the underestimation  $t_s$  counteracts the overestimation of the energy lost during relaxation, so that final effect on the sputtering cross section is small.

Considering the ESs also sheds light on the computational cost saved by assumption 3. Without assumption 3,  $t_s$  would depend on the exact times that each relaxation occurs. In this case, calculating the cross section would require integration over time for each excited ES considered. We have found that the consideration of 5 and 9 excited ESs are necessary to converge the cross sections of hBN and MoS<sub>2</sub> respectively (figure S1). For an N-point Gaussian quadrature, this would multiply the computational costs by  $N^5$  and  $N^9$  respectively. Assumption 3 removes this complication by eliminating the need to consider exactly when each relaxation happens. Instead, only the total number of relaxations before the PKA reaches  $d$  need be considered.

## S8 Calculating $E_{\min}$

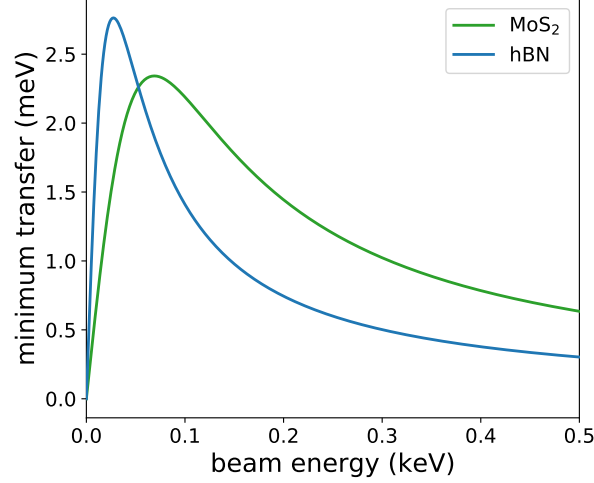


Figure S6: The minimum energy transfer from the beam electron to the target nucleus peaks at very low beam energies and is always much smaller than the nuclei's average thermal kinetic energy of  $\sim 39$  meV at room temperature.

In hBN, a unit cell contains a boron and nitrogen atom. As these atoms have similar masses and displacement thresholds (table 1), the sputtering of both atoms should be considered for a given beam energy. Thus, we approximate the maximum cross sectional area  $\sigma_{\max}$  of these atoms to be  $\Omega_{\text{hBN}}/2$ , where  $\Omega_{\text{hBN}}$  is the area of the hBN unit cell. On the other hand, molybdenum is much heavier than sulfur and has a much larger displacement threshold in MoS<sub>2</sub>.<sup>8</sup> This means that only the sputtering of sulfur needs to be considered. Additionally, of the two sulfur atoms in the MoS<sub>2</sub> unit cell, only the atom on the outgoing surface is eligible to sputter from a pristine system.<sup>8</sup> Therefore,  $\sigma_{\max}$  for sulfur sputtering from MoS<sub>2</sub> is  $\Omega_{\text{MoS}_2}$ , the area of the MoS<sub>2</sub> unit cell.

To approximate  $E_{\min}$ , we use the Rutherford displacement cross section<sup>9–11</sup> as an approximation to equation (2),

$$\sigma_R = \pi \left( \frac{Z\alpha}{|\mathbf{p}|\beta} \right)^2 \left( \frac{E_{\max}}{E_d} - 1 \right). \quad (\text{S19})$$

Setting  $\sigma_R = \sigma_{\max}$  and  $E_d = E_{\min}$  and solving for  $E_{\min}$  yields

$$E_{\min}(\epsilon_b) = E_{\max} \left[ \frac{\Omega}{\pi} \left( \frac{|\mathbf{p}_b|\beta}{Z\alpha} \right)^2 + 1 \right]^{-1}. \quad (\text{S20})$$

Using the Rutherford cross section instead of the McKinley-Feshbach cross section should be accurate for small beam energies for which  $\beta \ll 1$ . This makes it well-suited for finding  $E_{\min}$ , since  $E_d(n_f) < E_{\min}$  only for large  $n_f$ , and large  $n_i$  (and thus  $n_f$ ) are much more likely for small beam energies (figure 3).

With that said, the sputtering cross section is fairly insensitive to the exact value of  $E_{\min}$  when  $E_{\min} \ll E_{\max}$ . This is because the post-collision velocity of the PKA diminishes when the energy transfer  $E$  shrinks. The beam-induced excitations therefore have more time to relax before the PKA reaches the step in the energy surface (section 2.2.1). This makes  $P_f$  small for small  $E$ , so that contributions to the integral in equation (3) are extremely tiny for  $E$  near  $E_{\min}$ . As a result, changes in  $E_{\min}$  are essentially immeasurable for beam energies greater than 1 keV. Nonetheless, the use of  $E_{\min}$  is necessary for the calculation of a finite sputtering cross section.

## References

- [1] Peskin, M. E.; Schroeder, D. V. *An Introduction to Quantum Field Theory*, 1st ed.; Perseus Books Publishing, L.L.C.: Reading, MA, 1995.
- [2] Lancaster, T.; Blundell, S. J. *Quantum Field Theory for the Gifted Amateur*, 1st ed.; Oxford University Press: New York, NY, United States of America, 2014; p 350.
- [3] Bjorken, J. D.; Drell, S. D. *Relativistic Quantum Mechanics*; International series in pure and applied physics; McGraw-Hill, 1964.
- [4] Inc., W. R. Mathematica, Version 12.3. <https://www.wolfram.com/mathematica>.
- [5] Bethe, H. Zur Theorie des Durchgangs schneller Korpuskularstrahlen durch Materie. *Ann. Phys.* **1930**, *397*, 325–400.
- [6] Susi, T.; Meyer, J. C.; Kotakoski, J. Quantifying Transmission Electron Microscopy Irradiation Effects Using Two-Dimensional Materials. *Nat. Rev. Phys.* **2019**, *1*, 397–405.
- [7] Kretschmer, S.; Lehnert, T.; Kaiser, U.; V. Krashennnikov, A.; Krashennnikov, A. V. Formation of Defects in Two-Dimensional MoS<sub>2</sub> in Transmission Electron Microscope at Electron Energies Below the Knock-On Threshold: The Role of Electronic Excitations. *Nano Lett.* **2020**, *20*, 2865–2870.
- [8] Komsa, H. P.; Kotakoski, J.; Kurasch, S.; Lehtinen, O.; Kaiser, U.; Krashennnikov, A. V. Two-Dimensional Transition Metal Dichalcogenides Under Electron Irradiation: Defect Production and Doping. *Phys. Rev. Lett.* **2012**, *109*, 035503–1–5.
- [9] Thornton, S. T.; Marion, J. B. *Classical Dynamics of Particles and Systems*, 5th ed.; Brooks/Cole: Boston, MA, 2004.
- [10] Sakurai, J. J.; Napolitano, J. *Modern Quantum Mechanics*, 2nd ed.; Pearson Education: San Francisco, CA, 2011.
- [11] Yoshimura, A.; Lamparski, M.; Kharche, N.; Meunier, V. First-Principles Simulation of Local Response in Transition Metal Dichalcogenides under Electron Irradiation. *Nanoscale* **2018**, *10*, 2388–2397.